

# Biologically Inspired Blind Quality Assessment of Tone-Mapped Images

Guanghui Yue, Chunping Hou, Ke Gu , Shasha Mao, and Wenjun Zhang, *Fellow, IEEE*

**Abstract**—Currently, many tone mapping operators (TMOs) have been provided to compress high dynamic range images to low dynamic range (LDR) images for visualizing them on the common displays. Since quality degradation is inevitably induced by compression, how to evaluate the obtained LDR images is indeed a headache problem. Until now, only a few full reference (FR) image quality assessment metrics have been proposed. However, they highly depend on reference image and neglect human visual system characteristics, hindering the practical applications. In this paper, we propose an effective blind quality assessment method of tone-mapped image without access to reference image. Inspired by that the performance of existing TMOs largely depend on the brightness and chromatic and structural properties of a scene, we evaluate the perceptual quality from the perspective of color information processing in the brain. Specifically, motivated by the physiological and psychological evidence, we simulate the responses of single-opponent (SO) and double-opponent (DO) cells, which play an important role in the processing of the color information. To represent the textural information, we extract three features from gray-level co-occurrence matrix (GLCM) calculated from SO responses. Meanwhile, both GLCM and local binary pattern descriptor are employed to extract texture and structure in the responses of DO cells. All these extracted features and associated subjective ratings are learned to reveal the connection between feature space and human opinion score. Extensive experiments demonstrate that the proposed method outperforms the state-of-the-art blind quality assessment methods and is comparable with the popular FR methods on two recently published tone-mapped image databases.

**Index Terms**—High dynamic range (HDR), image quality assessment (IQA), no/blind reference (NR), tone mapping operator (TMO).

Manuscript received January 25, 2017; revised May 15, 2017 and June 25, 2017; accepted July 13, 2017. Date of publication August 14, 2017; date of current version December 15, 2017. This work was supported by the National Natural Science Foundation of China under Grant 61471262, Grant 61520106002, Grant 61731003, and Grant 61703009. (Corresponding author: Ke Gu.)

G. Yue and C. Huo are with Tianjin University, Tianjin 300072, China (e-mail: yueguanghui@tju.edu.cn; hcp@tju.edu.cn).

K. Gu is with Beijing Key Laboratory of Computational Intelligence and Intelligent System, Faculty of Information Technology, Beijing University of Technology, Beijing 100124, China (e-mail: guke.doctor@gmail.com).

S. Mao is with the Nanyang Technological University, Singapore 639798 (e-mail: ssmao@ntu.edu.sg).

W. Zhang is with Shanghai Jiao Tong University, Shanghai 200240, China (e-mail: zhangwenjun@sjtu.edu.cn).

Color versions of one or more of the figures in this paper are available online at <http://ieeexplore.ieee.org>.

Digital Object Identifier 10.1109/TIE.2017.2739708

## I. INTRODUCTION

IN REAL scenes, the luminance variations possess large proportions, ranging from faint starlight to direct sunlight [1]. To accurately represent the wide range of natural scene, high dynamic range (HDR) images and HDR imaging system have been prevailing and developed. With a wider dynamic range, HDR images preserve a better contrast variation, leading to a higher degree of detail preservation. Although HDR obtains encouraging advantages, unfortunately, HDR displays have not been widely applied due to technical problems and production costs. Therefore, how to visualize HDR images on the common display devices is indeed a headache problem. To tackle this problem, an increasing number of tone mapping operators (TMOs) have been developed to convert HDR image to low dynamic range (LDR) image [2].

In the past decades, LDR images have dominated the viewing experience via displaying on the common monitors (with 8-b range). Due to the restricted 256 levels of intensity, it inevitably causes information loss by TMO. Moreover, the performance of TMOs is highly dependent on the image content; that is, one TMO cannot suit for all the images, but for special cases. Theoretically, an excellent TMO can reserve a broader sense of color temperature, color saturation, luminance, and details than a general one. To compare the performance across different TMOs and select the optimal one, a subjective evaluation procedure is required in the traditional method [3]. Although subjective evaluation directly represents the human feelings, it has fundamental limitations. On the one hand, it relies on a large number of participants, and thus, it is time consuming and expensive. On the other hand, it is difficult to reproduce and impossible to apply in online systems. Hence, it is important and urgent to develop a promising objective image quality assessment (IQA) method to automatically evaluate the performance of TMOs [4], [5].

In the past several years, IQA problems have become the focus and hot spot of research [6]. Generally, objective IQA methods can be categorized into three types, i.e., full reference (FR), reduced reference (RR), and no/blind reference (NR), according to the available information from the reference image. Strictly speaking, FR IQA methods are most mature among them. Until now, only a few FR IQA methods for tone-mapped images have been proposed, such as tone-mapped image quality index (TMQI) [4], TMQI-II [7], feature similarity index for tone-mapped images (FSITM) [8], and sparse-domain model for tone-mapped images (SMTI) [9]. Additionally, RR IQA metrics [10], [11], compared to FR IQA methods, requiring

significantly less information of the reference image are also with rapid development.

However, information about reference image, in practical situations, is not available on the receiving terminal. Therefore, designing an effective NR IQA algorithm, in the absence of the information from reference image, is necessary and meaningful for applications in real scenarios. Currently, NR IQA metrics can be classified into two categories, namely opinion-unaware and opinion-aware methods, depending on whether it relies on subjective score or not. Since the acquirement of subjective score is time consuming, it is important and encouraging to design an opinion-unaware NR method, which does not require subjective scores. Mittal *et al.* [12] designed a natural image quality evaluator (NIQE) by measuring the distance between natural scene statistic (NSS) model statistics and that of distorted image. Zhang *et al.* [13] further improved NIQE by introducing more quality-aware features and enhancing the influence of the local quality scores.

Although the motivation of designing opinion-unaware methods is encouraging, they are not competent to all IQA problems and their performance is general. Therefore, opinion-aware method, which usually requires subjective scores, is the mainstream of current research. At present, most existing opinion-aware methods require train-test procedure. In the training stage, perceptual features are extracted to represent the image quality, followed by a regression module to map the feature vector to subjective score space. In the testing stage, the features with the same categories of training stage are extracted and fed into the trained regression module to obtain the predicted score. It is not difficult to find that the performance of such methods highly depends on effectiveness of the extracted features. Currently, NSS features, image filter responses, image decompositions, and entropies are the most frequency used handcrafted features. For example, BIQI [14] extracted NSS features on the wavelet domain. Similarly, BLIINDS2 [15] extracted NSS features on discrete cosine transform domain and the image quality was estimated via Bayesian inference approach. Xue *et al.* [16] utilized the joint statistics of the Laplacian of Gaussian (LOG) response and magnitude amplitude to represent the image quality. Li *et al.* [17] took the parameters of Weibull distribution on gradient map and local binary pattern (LBP) on the texture map. Gu *et al.* [18] employed three groups of free energy theory inspired and human visual system (HVS) inspired features to build an effective NR IQA method. Specifically, the features were extracted using NSS model. Li *et al.* [19] analyzed the luminance and structural information by extracting LBP features and luminance histogram on local contrast normalization map. After feature extraction, a regression module, e.g., support vector regression (SVR) and  $k$ -nearest neighbor (KNN), is used to build the relationship between feature vector and subjective score space.

All the NR IQA above-mentioned metrics have achieved considerable success in evaluating the quality of natural scene images. However, as previously validated, they are not competent to tone-mapped image obtained from HDR image by TMOs (as discussed in Section IV). In this paper, we propose an effective blind IQA method for tone-mapped images by considering HVS characteristics. Compared to the popular FR IQA methods

(e.g., TMQI, TMQI-II, and FSITM), which pay attention to the structural fidelity and naturalness, the proposed method evaluates the image quality from the perspective of color information processing in human brain. The main contributions of this paper are listed as follows.

- 1) Considering that the tone-mapped images usually suffer from color and structure distortion, we decompose the image into surface and boundary components by simulating HVS characteristics.
- 2) In order to reflect the surface and boundary component changes in distorted image, we extract gray-level co-occurrence matrix (GLCM) and LBP feature maps on these components. To be more specific, three features, i.e., energy, correlation, and homogeneity, from GLCM matrix are used to reflect the textural and structural information of surface and boundary components. While, the LBP statistical features are employed to represent the structural information of boundary component.
- 3) Through comprehensive evaluations, we verify that the proposed method outperforms the state-of-the-art NR IQA methods and is comparable with popular FR methods on two public HDR databases.

The remainder of this paper is organized as follows. Section II introduces the background and motivation of this paper. In Section III, we describe the proposed method in detail. In Section IV, the experimental setup, results and analysis are described and discussed strictly. Finally, the conclusion and future works are given in Section V.

## II. BACKGROUND AND MOTIVATION

In this section, we will first give a brief introduction about HVS. Then, the announcements needed attention for tone-mapped IQA are highlighted and analyzed.

### A. Biological Mechanisms of Color Information Processing

The world we live in is rich and colorful. Animals are able to distinguish various objects via surface, color, shape, and depth in the visual scene. Through a long period of evolution, human beings form perfect HVS, which promotes human beings to recognize different objects and understand the world well. Because HVS, which is the final receiver of images, is critical to visual perception process, simulating the chromatic behaviors or HVS characteristics is regarded as the most approximate and effective measurements for solving IQA problems. With the rapid development of neuroscience and visual cognition theories, the mystery of HVS is being gradually unveiled. Currently, extensive physiological and psychological evidences have become available to help explain process of HVS. Fig. 1 is a basic flowchart of color information processing on HVS.

In detail, the light rays emitted from object first shine in the retina, where the light signals are converted to electrical signals through transduction by photoreceptors. Second, the outputs of photoreceptors are transferred to the ganglion cells by means of an intrinsic local neural network (ILNN). Then, the responses of ILNN form the first receptive field (RF) of the visual system. Next, the processed information is then relayed via the

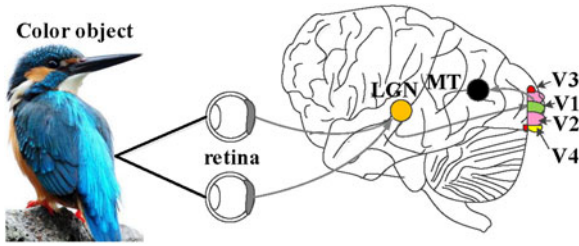


Fig. 1. Flowchart of color information processing on HVS.

lateral geniculate nucleus (LGN) to primary visual cortex (area V1) [20]. Finally, the signal further passes through the ventral pathway ( $V1 \rightarrow V2 \rightarrow V4 \rightarrow$  temporal lobe) and the dorsal pathway ( $V1 \rightarrow V2 \rightarrow MT \rightarrow$  parietal lobe) for further procession to form the appearance of the object in brain. Numerous studies [21], [22] have reported that the color information is transmitted along the retina  $\rightarrow$  LGN  $\rightarrow$  V1 pathway through two color opponent channels, i.e., blue–yellow (B–Y) channel and red–green (R–G). As the image distortion always induces the color changes, and thus, we pay more attention to the color information processing of HVS for IQA. The detailed functions of other visual areas (i.e., V2–V4 and MT) are outside the scope of this study, we do not revisit them in this paper.

Retina, as the vanguard for visual perception, converts light rays to electronic signals by photoreceptors. Totally, three kinds of cone photoreceptors, namely S, M, and L cones, are involved in retina to convert short, middle, and long wavelengths to electronic signals, respectively [23]. Then, the electronic signals are relayed to LGN, whose cells possess single-opponent (SO) RF. There are mainly two categories of SO cells in LGN. The first category has center-surround opponent RF, while that of secondary category has center-only opponent RF. It has been reported that the SO cells exhibit weak tuning for spatial opponency (i.e., orientation), but strong selectivity for color opponency (e.g., red versus green). Therefore, they are involved in the processing of surface information [24]. Subsequently, the responses of SO cells transmitted to V1. Compared to LGN, V1 area has more complex neurons and contains double-opponent (DO) RF, which are both chromatically and spatially opponent. In order words, DO RF tends to be responsive to both color and spatial opponency. Besides, some neurons in V1, called DO neurons, are orientation selective for both chromatic and achromatic patterns, which are considered to play a crucial role in boundary of color natural scenes. That is, DO cells are involved in the extraction of object boundary [25].

### B. Characteristic of Tone-Mapped Images

As previously mentioned, HDR image has larger range than LDR image. Therefore, they, to the greatest extent, preserves the naturalness, structure, and surface information of natural scene. On the contrary, LDR image usually losses structure and surface information, leading to unnatural perceptual effect. In order to better visualize the difference between HDR image and LDR image, we choose one HDR image and its corresponding LDR images from TMID database [4], as provided in Fig. 2. Note that the HDR image cannot display on the common monitor.

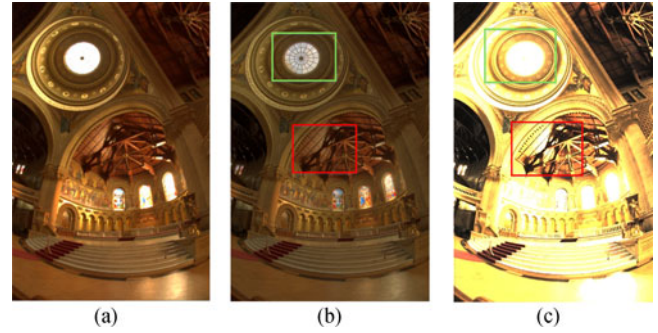


Fig. 2. Comparisons of HDR and LDR images: (a) A screenshot of original HDR image, (b) and (c) are two LDR images processed by different TMO operators. For the convenience of viewing, we label the obviously different regions with rectangles.

We directly capture it by a screenshot tool on the HDR shop [26] and attach it on this paper. As can be seen from Fig. 2, the tone-mapped image, due to the limitation of dynamic range, losses brightness and chromatic and structural information. For example, Fig. 2(b) is created by darkening Fig. 2(a), the region in red rectangle suffers from color distortion. Therefore, the surface of object changes. Similarly, when the brightness is enhanced unduly, the structure information is easily lost, as shown in the green rectangle marked region in Fig. 2(c). Note that the structure information of original HDR image is abundant. The structure loss, e.g., the structure of dome in Fig. 2(a), is due to the effect of common display. It is reasonable to suppose that a good tone-mapped image contains the original color and structure information.

Considering that the tone-mapped images are frequently distorted in forms of brightness and structure, we build an effective NR IQA method by analyzing the surface and boundary characteristics. To some extent, we can extract texture (structure) features to represent surface (boundary) characteristics. Motivated by the recently physiological findings, we decompose an image into two components (i.e., SO and DO) by simulating process of HVS on color image. Then, we extract texture features on the responses of SO, while extracting both texture and structure features on the responses of DO. Finally, the extracted features and the associated mean opinion scores (MOS) are fed into SVR to model the relationship from features to perceptual image quality. Through extensive experiments, we find that these features are sensitive to image distortions and effective to measure the perceptual quality of tone-mapped images.

### III. PROPOSED NR IQA SCHEME

Fig. 3 depicts the flowchart of the proposed NR IQA scheme. The proposed method is composed of two stages, namely training stage and testing stage. During training stage, the basic features are extracted from the responses of SO and DO cells. Then, an SVR module is learned to build the relationship between these features and subjective ratings. During testing stage, the basic features are first extracted. Subsequently, a represented score can be predicted by feeding these features into the learned SVR model. Totally, three procedures, namely image decomposition, feature extraction, and quality inference, are involved in



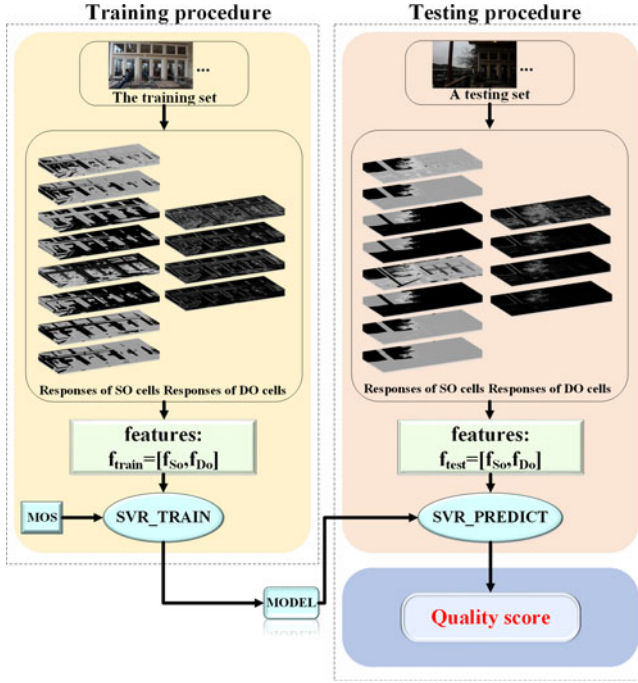


Fig. 3. Pipeline of the proposed method.

the proposed method. In this section, we introduce the proposed NR IQA scheme in detail.

### A. Image Decomposition

As reported previously, the biological mechanisms for color information processing is processed along the Retina-LGN-V1 visual pathway [21]. Therefore, we simulate the responses of LGN and V1 by mathematical formulas to evaluate the surface and structure distortions. It has been reported that there are two color opponent channels (R-G channel and B-Y channel) for transmitting color information in the visual pathway. Due to the imperfect wiring, the blue cones might mingle with green cones, leading to a noisy R-G channel. To solve this problem, a red-cyan (R-C) channel and a white-black (Wh-BI) channel were designed [27]. Whereby, the C channel is obtained by combining B and G channels; Wh and BI channels are obtained by combining the R, G, and B channels together.

The visual processing of color information starts at the photoreceptor layer of the retina. Specifically, cones, as a type of photoreceptor, are sensitive to light rays. Totally, there are three types of cones according to the most sensitive wavelength. Particularly, the L, M, and S cones are with preferable responses to the blue, green, and red colors, respectively. Given an input image  $I$ , its color information is first processed in a trichromatic via the three types of the cones. The response of cone on retina and can be formulated as follows:

$$G_{H_\nu} = H_\nu \cdot g(x, y, \sigma, \lambda, \psi), H_\nu \in \{R_\nu, G_\nu, B_\nu\} \quad (1)$$

where  $R_\nu$ ,  $G_\nu$ , and  $B_\nu$  are the image intensities of the red, green, and blue channels, respectively.  $g(x, y, \sigma, \lambda, \psi)$  is the Gabor filter to simulate the spatial sensitivity distributions of each individual color component [28]. It can be expressed as

follows:

$$g(x, y, \sigma, \lambda, \psi) = \exp\left(-\frac{\hat{x}^2 + \gamma^2 \cdot \hat{y}^2}{2\sigma^2}\right) \cdot \cos\left(2\pi \frac{\hat{x}}{\lambda} + \psi\right) \quad (2)$$

with

$$\hat{x} = x \cdot \cos \theta + y \cdot \sin \theta \quad (3)$$

$$\hat{y} = -x \cdot \sin \theta + y \cdot \cos \theta \quad (4)$$

where  $\gamma$  is used to control the ellipticity of Gabor function;  $\psi$  denotes the center frequency;  $\theta$  is the orientation angle; and  $\sigma$  is the standard deviation controlling the RF size of the cones. All filter parameters are adjusted so that the tuning properties of the corresponding units match the bulk of V1 parafoveal simple cells [29]. However, it is out of scope to study the impacts of these parameters on the Gabor function. In this paper, we strictly refer to [27] and [30] by setting  $g(x, y, \sigma, \lambda, \psi)$  as a rectangle template with  $\gamma = 0.3$ ,  $\lambda = 5.64$ ,  $\sigma = 4.51$ , and  $\psi \in \{0^\circ, 90^\circ\}$ . In [27] and [30], these parameters have a certain relationship with  $\lambda = 2 \cdot R_f / 3.9$  and  $\sigma = \lambda \cdot 0.8$ , where  $R_f$  is the filter size. With such constraints, the filter size is the only parameter that may affect the final performance. In this paper, we set  $R_f$  with a size of  $11 \times 11$  pixels via experiments discussed in Section IV-C. To form excitatory/inhibitory center or surround structures, these distributions should obtain the ability of isolating the positive/negative subunits from linear oriented filters. Therefore, the Gabor function is further modified as follows:

$$g^p = \begin{cases} g(x, y, \sigma, \lambda, \psi), & \text{if } g(x, y, \sigma, \lambda, \psi) > 0 \\ 0, & \text{otherwise} \end{cases} \quad (5)$$

$$g^n = \begin{cases} g(x, y, \sigma, \lambda, \psi), & \text{if } g(x, y, \sigma, \lambda, \psi) \leq 0 \\ 0, & \text{otherwise} \end{cases} \quad (6)$$

where  $g^p$  ( $g^n$ ) is the modified Gabor filter to form excitatory (inhibitory) response. With such operation,  $G_{H_\nu}$  contains both excitatory and inhibitory responses of cone.

Then, four pairs of single opponent color channels (i.e., R-G, R-C, Y-B, and Wh-BI) are created by using linear combinations of the responses of the filtered color channels

$$S = \begin{bmatrix} S_{R \pm G} \\ S_{R \pm C} \\ S_{Y \pm B} \\ S_{Wh \pm BI} \end{bmatrix} = \begin{bmatrix} \pm \frac{1}{\sqrt{2}} & \mp \frac{1}{\sqrt{2}} & 0 \\ \pm \frac{2}{\sqrt{6}} & \mp \frac{2}{\sqrt{6}} & \mp \frac{2}{\sqrt{6}} \\ \pm \frac{1}{\sqrt{6}} & \pm \frac{1}{\sqrt{6}} & \mp \frac{1}{\sqrt{6}} \\ \pm \frac{1}{\sqrt{3}} & \pm \frac{1}{\sqrt{3}} & \pm \frac{1}{\sqrt{3}} \end{bmatrix} \cdot \begin{bmatrix} G_{R_\nu} \\ G_{G_\nu} \\ G_{B_\nu} \end{bmatrix} \quad (7)$$

In (7), the  $g^p$  ( $g^n$ ) is used in computation when “+” (“−”) sign is selected. That is, the excitatory (inhibitory) response of cone is involved in the operation.

In order to maintain positive firing rates, we rectify the response ( $S$ ) via half-squaring [31]. Besides, the divisive normalization circuit, which was originally proposed to the contrast response of cells in the primary visual cortex, was applied to color processing [32]. The corresponding response

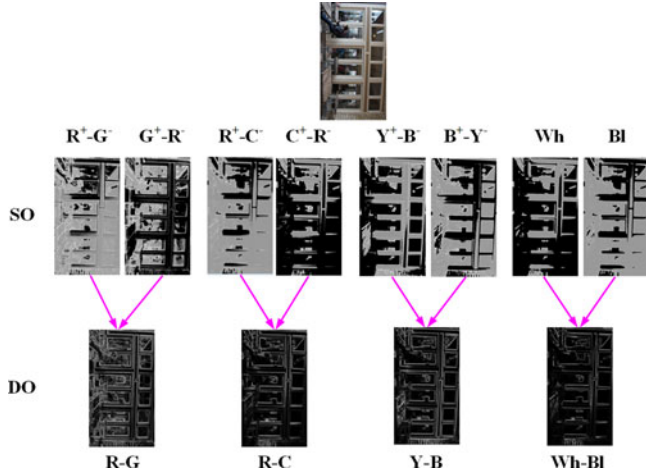


Fig. 4. Process of color image decomposition by the SO and DO color channels. The first row gives the color image; the second row lists the response maps of SO cells; and the third row posts up the response maps of DO cells.

can be described as follows:

$$\kappa(c) = \sqrt{\frac{k \cdot \varsigma(c)}{\delta^2 + \sum \varsigma(c)}}, c \in \{R \pm B, R \pm C, Y \pm B, Wh \pm Bl\} \quad (8)$$

where  $\varsigma(c)$  indicates the response of half-squared filter for the opponent channel  $c$ ;  $\delta$  and  $k$  are the constant scale factor and the semisaturation constant, respectively. The summation symbol  $\sum$  is utilized to sum half-squared filter responses with similar tuning parameters across all color channel. We directly follow the neuroscience data [33] and set the parameters (i.e.,  $k$  and  $\delta$ ) as 1 and 0.0225, respectively.

In the cortex layer of V1, the DO cells were almost all color-luminance cells. The RFs of most color- and color-luminance-sensitive neurons are both chromatically and spatially opponent. Unlike the SO channels, the DO channels contain both center and surround (excitatory/inhibitory) subunits. Therefore, we directly filter the SO responses ( $\kappa(c)$ ) with spatial sensitivity function  $g(x, y, \sigma, \lambda, \psi)$  and sum the responses of opponent color channel pairs together to obtain the DO responses ( $D$ )

$$D(RB) = \kappa(R + B) \cdot g(x, y, \sigma, \lambda, \psi) + \kappa(R - B) \cdot g(x, y, \sigma, \lambda, \psi) \quad (9)$$

where  $D(RB)$  is the DO response of R-B channel. The other three channels can also be calculated using (9). Similar to SO cells, the responses of DO cells are further rectified via half-squaring. Toward this end, four response maps of DO cells can be obtained for an input image, as shown in Fig. 4. The procedure of the image decomposition is summarized in Algorithm 1.

## B. Feature Extraction

After obtained previously, the responses of SO and DO cells are highly simulated. Fig. 4 depicts the flowchart of color image decomposition. As shown in Fig. 4, the response of SO cell reflects the surface information to some extent [27], and thus,

### Algorithm 1: Image Decomposition.

- 1: Input: color image  $I$ .
- 2: Obtain the response ( $G_{H_v}$ ) of pyramidal cell on retina using Eq. (1).
- 3: Obtain the response ( $\kappa(c)$ ) of SO through:
  - calculate four pairs of single opponent color channels using Eq. (7);
  - rectify the response  $S$  via half-squaring and normalization using Eq. (8).
- 4: Obtain the response of DO using Eq. (9) and half-squaring.
- 5: Output: responses of SO and DO.

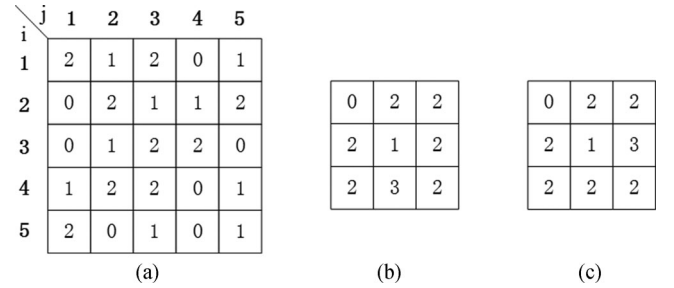


Fig. 5. GLCM. (a) A matrix with size  $5 \times 5$ . (b)  $M_{1,135^\circ}$  of the matrix in (a). (c)  $M_{1,315^\circ}$  of the matrix in (a).

we employ GLCM descriptor to extract textural information of SO response. The GLCM is composed of the joint probability density between the gray levels of image [34]. First, the image  $I$  is quantized to  $L$  gray values and formed the converted matrix  $C_I$ . Then, the number of occurrences of the pair of gray values  $i$  and  $j$  being a neighbor with distance  $d$  in the direction of  $\theta$  in  $C_I$  is expressed as  $m_{d,\theta}(i, j)$  ( $i = 1, 2, \dots, L; j = 1, 2, \dots, L$ ). Finally, the co-occurrence matrix obtained from spatial distance parameter  $d$  and angle  $\theta$  is denoted as  $M_{d,\theta}$ . According to the definition, it is not difficult to find that  $M_{d,\theta}$  and  $M_{d,\theta+180^\circ}$  have the same entries on the main diagonal and each reflecting the other entries with the main diagonal as axis of symmetry. That is,  $M_{d,\theta}(i, j) = M_{d,\theta+180^\circ}(i, j)^T$ . An example about GLCM generation with  $d = 1$  and  $L = 3$  is shown in Fig. 5.

Numerous features have been extracted to analyze image properties from GLCM map [34]. In this paper, we choose the following three features for IQA, namely contrast, energy, and homogeneity, which are simple yet achieving good performance. Among those three features, the contrast describes clarity of image. A clear image will obtain a big contrast. It can be expressed as follows:

$$G_C = \sum_{i=1}^L \sum_{j=1}^L (i - j)^2 \cdot P_{d,\theta}(i, j) \quad (10)$$

where  $P_{d,\theta}(i, j)$  denotes the probability of an entry  $m_{d,\theta}(i, j)$  in  $M_{d,\theta}$ , and can be formulated as follows:

$$P_{d,\theta}(i, j) = m_{d,\theta}(i, j) / \sum_{i=1}^L \sum_{j=1}^L m_{d,\theta}(i, j). \quad (11)$$

Energy describes whether the overall image has a uniform distribution as well as its roughness. A small energy value indicates that the image possesses uniform distribution and fine texture. Formally, it can be defined as follows:

$$G_E = \sum_{i=1}^L \sum_{j=1}^L P_{d,\theta}(i, j)^2. \quad (12)$$

Homogeneity is local image descriptor, which describes local gray correlation. Concretely, homogeneity measures local change of image. The image with small local change will obtain a large value of homogeneity. The homogeneity can be calculated as follows:

$$G_H = P_{d,\theta}(i, j)/(1 + |i - j - 2|). \quad (13)$$

As discussed previously, the selective three features of GLCM achieve the combination of local and global features and can represent the textural information. In this paper, we extract these features with distance as 1 in four directions ( $0^\circ$ ,  $45^\circ$ ,  $90^\circ$ , and  $135^\circ$ ) for each SO response. Toward this end, we totally extract 96 features ( $f_{SO}$ ) of SO responses.

Since the response of DO cell reflects the structure and boundary [27], we utilize LBP descriptor to extract the structural information of DO responses. As DO response is computed based on SO response, we also pay attention to the textural information and utilize GLCM descriptor to extract the textural information of DO response. LBP is a kind of operator used to describe the local structure feature of the image [35]. It is proposed to describe the relationship between the center pixel ( $n_c$ ) and surrounding neighbors ( $n_i$ ) by computing gray-level difference

$$\text{LBP}_{P,R} = \sum_{i=0}^{P-1} s(I(n_i), I(n_c)) \cdot 2^i \quad (14)$$

where  $I(n_c)$  denotes the gray value of center pixel ( $n_c$ ), while  $I(n_i)$ ,  $i = \{0, 1, 2, 3, \dots, P-1\}$  denotes the gray value of circularly symmetric neighbor pixel ( $n_i$ );  $P$  is the number of sampling point, which controls the quantization of the angular space.  $R$  is the radius of the neighbors that determines the spatial resolution of the operator.  $s(\cdot, \cdot)$  is the thresholding function of LBP, which can be expressed as follows:

$$s(I(n_i), I(n_c)) = \begin{cases} 1, & \text{if } I(n_i) - I(n_c) \geq 0 \\ 0, & \text{if } I(n_i) - I(n_c) < 0. \end{cases} \quad (15)$$

Then, the rotation invariant uniform LBP can be formulated as follows [35]:

$$\text{LBP}_{P,R}^{\text{riu2}} = \begin{cases} \sum_{i=0}^{P-1} s(I(n_i), I(n_c)), & \text{if } \mu(\text{LBP}_{P,R}) \leq 2 \\ P+1, & \text{otherwise} \end{cases} \quad (16)$$

where the superscript *riu2* denotes the rotation invariant uniform patterns when the uniform measure  $\mu$  is less than 2. Formally,

$\mu$  is calculated as the number of bitwise transitions

$$\mu(\text{LBP}_{P,R}) = \|s(I(n_{P-1}), I(n_c)) - s(I(n_0), I(n_c))\| + \sum_{i=1}^{P-1} \|s(I(n_i), I(n_c)) - s(I(n_{i-1}), I(n_c))\|. \quad (17)$$

From (16) and (17), it can be intuitively observed that the uniform LBP map would have  $P+2$  patterns. There are two essential parameters, (i.e., radius  $R$  and sampling points  $P$ ) determining the characteristics of LBP descriptor. In this paper, we set  $R$  and  $P$  as 1 and 8 (discussed in Section IV-C), respectively. As a result, ten features can be obtained from each LBP map. Because we have obtained four responsive maps of DO cells, 48 (40) features can be extracted via GLCM (LBP) operation. At the end, we totally extract 88 features ( $f_{DO}$ ) of DO responses. Overall, combining  $f_{SO}$  and  $f_{DO}$  together, we extract 184 features in total to reflect the degree of distortion.

### C. Quality Inference

Broadly speaking, many training-based NR IQA metrics operate in two stages, e.g., training stage and testing stage. Given a database, it is randomly divided into two portions, training portion and testing portion. During the training stage, features ( $f_{\text{train}}$ ) of training portion are first extracted. Then, the model is acquired via machine learning methods (such as SVR) on the extracted features ( $f_{\text{train}}$ ) and the associated subjective MOS. During the testing stage, features ( $f_{\text{test}}$ ) of testing portion are first extracted. Then, predicted scores of testing portion are obtained by feeding the features ( $f_{\text{test}}$ ) into the trained model. In other words, the image quality can be predicted by using the trained model. Since SVR [36] has been widely proved to be efficient in NR IQA [17], [18]. Therefore, in this paper, we follow the previous works (e.g., [15], [16], [37], and [38]) and choose the Library for Support Vector Machines (LIBSVM) package (a simple and easy-to-use support vector machines tool designed by Lin for classification and regression) with radial basis function kernel for predicting image quality [39].

## IV. EXPERIMENTAL RESULTS AND ANALYSIS

In this section, we first introduce the experimental protocol. Then, the effectiveness of the proposed method is validated through extensive comparisons. Additionally, the analysis about the achieved performance is conducted.

### A. Experimental Protocol

In order to verify the effectiveness and robustness of the proposed method, we make comparisons between our method and the state-of-the-art NR IQA metrics and popular FR IQA metrics on the following public HDR databases.

- 1) TMID database [4]: This database was developed by researchers at the University of Waterloo, Waterloo, ON, Canada. A total of 120 tone-mapped LDR images were created from 15 HDR images via eight different TMOs. The subjective scores are in the form of MOS, which are computed as the mean value of subjective scores from 20



observers. The MOS ranges from 1 to 8, corresponding the best to worst perceptual quality.

- 2) ESPL-LIVE HDR Database [40]: This database was built by Laboratory for Image & Video Engineering at the University of Texas, Austin, TX, USA. Totally, 1811 images, composed of three groups (i.e., tone-mapped LDR images, multiexposure fusion images, and postprocessing images by software), involve in this database. The perceptual quality of each image is evaluated by numerous qualified observers over the crowdsourcing platform. On the average, the MOS of each image is obtained by 110 subjects. Until now, to the best of our knowledge, it is the largest and most credible database in HDR IQA area.

Four commonly used performance criteria, suggested by video quality experts group (VQEG), are employed to evaluate and compare the proposed method with existing IQA methods. First of all, Pearson linear correlation coefficient (PLCC), which reflects the accuracy of the prediction, can be calculated as follows:

$$\text{PLCC} = \frac{\sum_{i=1}^n (\rho_i - \bar{\rho}) \cdot (\nu_i - \bar{\nu})}{\sqrt{\sum_{i=1}^n (\rho_i - \bar{\rho})^2} \cdot \sqrt{\sum_{i=1}^n (\nu_i - \bar{\nu})^2}} \quad (18)$$

where  $\{\rho_1, \rho_2, \dots, \rho_n\}$  represent the subjective ratings of tested images with number of  $n$ , while  $\{\nu_1, \nu_2, \dots, \nu_n\}$  denote associated predicted scores. To specify,  $\rho_i$  is the subjective score of the  $i$ th image and  $\nu_i$  is the corresponding predicted score;  $\bar{\rho}$  and  $\bar{\nu}$  are the associated mean values of subjective scores and predicted scores of the tested images.

Second, the root-mean-squared error (RMSE) is computed to reflect the prediction consistency

$$\text{RMSE} = \sqrt{\frac{1}{n} \sum_{i=1}^n (\rho_i - \bar{\nu})^2}. \quad (19)$$

Third, to evaluate the prediction monotonicity, Spearman rank correlation coefficient (SRCC) is expressed as follows:

$$\text{SRCC} = 1 - \frac{1}{n \cdot (n-1)} \cdot \sum_{i=1}^n (K_i - \Gamma_i)^2 \quad (20)$$

where  $\Gamma_i$  and  $K_i$  are the  $i$ th converted ranks of predicted scores and corresponding subjective scores.

Finally, Kendall's rank correlation coefficient (KRCC) is given as follows:

$$\text{KRCC} = \frac{2 \cdot (N_c - N_d)}{n \cdot (n-1)} \quad (21)$$

where  $N_c$  and  $N_d$  stand for the number of concordant and discordant pairs in the database, respectively.

With experience, higher values of PLCC, SRCC, and KRCC, unlike that of RMSE, indicate a superior performance of the tested metric. According to VQEG, a five logistic regression procedure is required, before the calculation of PLCC and RMSE, to remove the nonlinearity of objective quality predictions

$$q_{\text{VQEG}} = \xi_1 \cdot \left( \frac{1}{2} - \frac{1}{1 + e^{\xi_2 \cdot (v_o - \xi_3)}} \right) + \xi_4 + \xi_5 \quad (22)$$

where  $v_o$  and  $q_{\text{VQEG}}$ , respectively, denote the objective values (i.e., the predicted scores) and mapped scores;

$\{\xi_1, \xi_2, \dots, \xi_5\}$  as the model parameters, can be obtained numerically via a nonlinear regression process.

## B. Overall Performance Comparison

To investigate the effectiveness of the proposed method, we make comparisons between the proposed method with popular FR and state-of-the-art NR IQA methods on the two HDR databases mentioned previously. The selected FR metrics are MSSIM [41], TMQI [4], TMQI-II [7], SMTI [9], and FSITM [8]. The selected NR IQA methods compose of opinion-unaware methods, including NIQE [12] and ILNIQE [13], and opinion-aware methods, including BIQI [14], HOSA [42], FISH [43], BLIINDS2 [15], BRISQUE [37], GM-LOG [16], SISLBM [44], SSEQ [38], TCLT [45], NFERM [18], NRSL [19], and BSD [17]. For no training-based methods, the score of each image in the database is computed directly. Subsequently, the selected four criteria are calculated across all the computed scores of images and the associated MOS. On the contrary, the training-based metrics consist of two portions, i.e., training stage and testing stage. The training stage is used to determine the model, while the testing stage is used to validate the performance. It is no doubt that the performance results may be affected by the train-test separation. To avoid the bias of specific train-test splits, we follow other training-based methods by repeating the train-test split procedure 1000 times randomly [16]–[19], [38]. In this paper, the database is split into 80% training portion and 20% testing portion as [16]–[19], [38]. In order to avoid the unnecessary mistakes, all the results except SMTI and FSITM are obtained by running the demos released by authors. Note that we fail to obtain the source codes of SMTI and FSITM, therefore, we directly copy the results from [9] and [8]. As the ESPL-LIVE HDR database does not release the reference images, and thus, we do not operate the FR metrics on it. To ensure the fairness of comparison, the network is optimized by selecting the optimal parameters to achieve the best performance for each training-based method. To be specific, these parameters are determined by seeking the minimum error between the predicted and original scores over the whole database before the train-test split procedure.

Table I tabulates the experimental results, which are denoted in forms of median value, on TMID and ESPL-LIVE HDR databases. We highlight the top one by bold type to facilitate observation on each type. From the table, some meaningful phenomenon can be intuitively observed. First of all, the performance of all metrics on TMID database is superior to those on ESPL-LIVE HDR database. In particular, most metrics get soddish results on ESPL-LIVE HDR database, e.g., NIQE, SISLBM, and ILNIQE. And then, the training-based methods basically outperform the no training-based methods on both databases. Specifically, some training-based metrics, e.g., GM-LOG, SSEQ, and NRSL, obtain encouraging performance with PLCC exceeding 0.65. Next, the performance of some metrics, such as BLIINDS2 and BSD, has tremendous difference between two databases. As a result, they are in lack of universality, hindering their wide application. In addition, the proposed method is comparable with the selected FR methods. In all FR

**TABLE I**  
PERFORMANCE COMPARISONS BETWEEN THE PROPOSED METHOD WITH STATE-OF-THE-ART NR IQA METRICS  
ON TWO TONE-MAPPED IMAGE DATABASES

Metrics	Type	TMID [4]				ESPL-LIVE HDR [40]			
		PLCC	SRCC	KRCC	RMSE	PLCC	SRCC	KRCC	RMSE
MSSIM [41]	FR	0.3424	0.1804	0.1232	1.8074	–	–	–	–
TMQI [4]	FR	<b>0.7716</b>	0.7407	0.5588	<b>1.2236</b>	–	–	–	–
TMQI-II [7]	FR	0.7240	0.6578	0.4888	1.3342	–	–	–	–
SMTI [9]	FR	–	<b>0.8606</b>	<b>0.7508</b>	–	–	–	–	–
FSITM [8]	FR	–	0.8095	0.7143	–	–	–	–	–
NIQE [12]	NR	0.4090	0.4522	0.3191	1.7555	0.0768	0.0904	0.0603	10.001
ILNIQE [13]	NR	0.3456	0.2512	0.1680	1.8053	0.2678	0.2259	0.1509	9.4462
HOSA [42]	NR	0.4007	0.3507	0.2431	1.7625	0.1751	0.1622	0.1063	9.8755
FISH [43]	NR	0.3215	0.2440	0.1629	1.8216	0.1535	0.1423	0.0937	9.9115
BIQI [14]	NR	0.3456	0.2854	0.1905	1.8054	0.1734	0.1657	0.1100	9.8784
BLINDS2 [15]	NR	0.5330	0.4683	0.3265	1.6277	0.1434	0.0379	0.0254	10.210
BRISQUE [37]	NR	0.7716	0.6056	0.4218	1.2369	0.3901	0.3493	0.2367	9.2159
GM-LOG [16]	NR	0.8065	0.6425	0.4554	1.1430	0.5075	0.4993	0.3458	8.6135
SISLBM [44]	NR	0.1098	0.1222	0.0847	1.9121	0.1426	0.2010	0.1333	9.9279
SSEQ [38]	NR	0.6578	0.5011	0.3666	1.4545	0.5387	0.5327	0.3693	8.4152
TCIT [45]	NR	0.3301	0.2511	0.1920	1.1859	0.2541	0.2508	0.1690	9.7013
NFERM [18]	NR	0.6270	0.4588	0.3261	1.1813	0.4870	0.4789	0.3293	8.7292
NRSL [19]	NR	0.7411	0.6225	0.4644	1.2945	0.5516	0.5415	0.3805	8.3291
BSD [17]	NR	0.7227	0.6157	0.4380	1.1325	0.3827	0.3747	0.2532	9.2381
Proposed	NR	<b>0.8243</b>	<b>0.7321</b>	<b>0.5481</b>	<b>1.1015</b>	<b>0.7019</b>	<b>0.6915</b>	<b>0.4989</b>	<b>7.1327</b>

methods, SMTI and FSITM occupy the top two positions. Last but not the least, the proposed method achieves considerable results and outperforms all competing NR methods. In other words, our method can well estimate the perceptual quality and is consistent with subjective ratings.

Reasonable explanations of these can be attributed to the following. First, compared to TMID, ESPL-LIVE HDR database also contains multiexposure fusion images and postprocessing images by software apart from tone-mapped images. That is, it is more complex and increases the difficulty of IQA task. Therefore, it is no doubt that most metrics fail in evaluating the perceptual quality of image in ESPL-LIVE HDR database; second, most no training-based methods, e.g., SISLBM, NIQE, and ILNIQE, employed NSS features or features extracted in transform domain. Such features are extracted after analyzing the distortion characteristics, followed by a combined procedure of features to obtain the predicted score. Hence, they are more suitable for image distorted by common distortions, including white noise, compression, and blur, while perform badly on tone-mapped images; third, on the contrary, the training-based methods require no combined procedure, but build the mapping model from feature space to subjective ratings through supervised neural networks, such as SVR and KNN. As the relationship between features and subjective ratings is extremely complex, a training procedure has more advantages than simple combined procedure. As a result, it is natural that the training-based methods are superior to no training-based methods. Fourth, compared to NR metric, FR metric has reference image, and thus, it is easy to obtain higher performance. Since SMTI considers more on HVS, it is better than the other three FR metrics. Besides, as the TMQI-II is more sensitive to hardly noticeable and unnoticeable differences in TMOs processed images, compared with TMQI and FSITM, it is not suitable for comparison of results of different TMOs [46]. Finally, considering that tone-mapped

**TABLE II**  
PERFORMANCE ON BOTH DATABASES WITH VARIOUS TRAIN-TEST SPLITS

Metrics	TMID [4]				ESPL-LIVE HDR [40]			
	PLCC	SRCC	KRCC	RMSE	PLCC	SRCC	KRCC	RMSE
SO <sup>1</sup>	0.6351	0.5296	0.3811	1.4754	0.6032	0.5960	0.4140	7.9889
DO <sup>2</sup>	0.7891	0.6652	0.4873	1.1963	0.5650	0.5493	0.3860	8.2682
Overall <sup>3</sup>	<b>0.8243</b>	<b>0.7321</b>	<b>0.5481</b>	<b>1.1015</b>	<b>0.7019</b>	<b>0.6915</b>	<b>0.4989</b>	<b>7.1327</b>

<sup>1</sup> “SO” means that a method uses only surface features  $f_{SO}$ .

<sup>2</sup> “DO” means that a method uses only boundary features  $f_{DO}$ .

<sup>3</sup> “Overall” denotes the proposed method that uses both surface and boundary features.

images suffer from brightness and structure distortions, the proposed method decompose the image into surface and boundary components by simulating HVS characteristics. Subsequently, the GLCM and LBP descriptors are utilized to extract textural and structural information. To this end, the proposed method gets considerable results and solves the IQA problem for tone-mapped images effectively.

As mentioned previously, the proposed method comprehensively consider the characteristics of color and boundary. Therefore, it is meaningful and interesting to explore the contribution of each decomposed component, which respectively represents the surface and boundary, on the final performance. In view of this, we conduct an extra experiment to unveil the mystery. Table II lists the experimental results, which are determined as the median values after 1000 iterations of train-test splits. In the table, “SO” uses only surface features and “DO” utilizes only boundary features in Section III. As expected, both components have positive effects on the final results. Taking Table I for comparison, it can be obviously observed that the performance of each component can reach the top three positions (compared with NR metrics) on both databases. Moreover, their impacts



**TABLE III**  
RESULTS OF THE PROPOSED METHOD WITH DIFFERENT PARAMETERS ON BOTH DATABASES

Model	TMID [4]				ESPL-LIVE HDR [40]			
	PLCC	SRCC	KRCC	RMSE	PLCC	SRCC	KRCC	RMSE
Contrast	0.7461	0.6126	0.4364	1.2767	0.5219	0.5139	0.3569	8.5255
Energy	0.7966	0.7113	0.5263	1.1755	0.6761	0.6600	0.4748	7.3743
Homogeneity	0.8083	0.6944	0.5177	1.1315	0.5305	0.5242	0.3641	8.5005
R1P8	0.8201	0.7246	0.5382	1.1187	0.7012	0.6891	0.4982	7.1398
R2P8	0.8308	0.7290	0.5448	1.0653	0.6976	0.6881	0.4963	7.1546
R3P8	0.8291	0.7240	0.5402	1.0742	0.6949	0.6868	0.4953	7.1907
R4P8	0.8294	0.7270	0.5428	1.0795	0.6969	0.6883	0.4967	7.1706
R1P4	0.8188	0.7328	0.5501	1.1152	0.6822	0.6713	0.4821	7.3229
R1P16	0.8252	0.7289	0.5382	1.1024	0.7029	0.6921	0.5003	7.1097
$R_f$ 7	0.8200	0.7033	0.5282	1.1125	0.6532	0.6420	0.4537	7.5787
$R_f$ 11	0.8243	0.7321	0.5481	1.1015	0.7019	0.6915	0.4989	7.1327
$R_f$ 15	0.8209	0.7224	0.5382	1.1116	0.6945	0.6562	0.4934	7.1454
$R_f$ 19	0.8054	0.6981	0.5137	1.1247	0.6956	0.6589	0.4956	7.1422

on two databases are different. Particularly, the DO contributes more on TMID database, while it plays a secondary role in ESPL-LIVE HDR database. Overall, the performance increases greatly when combine the two portions together, represented as “overall” in Table II.

### C. Parameters Sensitivity

In the feature extraction stage, the proposed method totally extracts two categories of features, i.e., GLCM and LBP. Considering the definitions of these features, (i.e., contrast, energy, and homogeneity as shown in (10)–(13), these features in  $0^\circ$ ,  $45^\circ$ ,  $90^\circ$ , and  $135^\circ$  can also reflect those in  $180^\circ$ ,  $225^\circ$ ,  $270^\circ$ , and  $315^\circ$ . Generally speaking, the computation of GLCM with distance 1 and directions ( $0^\circ$ ,  $45^\circ$ ,  $90^\circ$ , and  $135^\circ$ ) is indeed enough to reflect the spatial relationship between the center pixel and its neighborhoods. Therefore, we do not consider the impacts of generation step and direction on the overall performance, but pay more attention on exploring the individual effects of the extracted contrast, energy, and homogeneity. Similarly, the radius  $R$  and sampling points  $P$  determine the spatial resolution of the LBP descriptor. In order to explore the importance of these two parameters, we test the performance of the proposed method with different LBP radiuses (sampling points), ranging from 1 (4) to 4 (16). When explore one parameter’s impact, other parameters are fixed. In addition, we also make an attempt to explore the impacts of Gabor function’s filter size  $R_f$  on the final performance. Table III summarizes the experimental results on both databases. In Table III, contrast denotes one proposed method that only utilizes contrast of GLCM and all features of LBP [when the radius (sampling point) is 1 (8)] as features. Such arrangement also applies to energy and homogeneity.  $R_h Pl$  ( $h \in \{1, 2, 3, 4\}$ ,  $l \in \{4, 8, 16\}$ ) denotes one proposed method that uses all features of GLCM and features of LBP when the radius (sampling point) is  $h$  ( $l$ ).  $R_f b$  ( $b \in \{7, 11, 15, 19\}$ ) indicates the proposed method when the  $R_f$  is set as  $b$ . From Table III, we have the following observations. First, when only utilizing single feature of GLCM, the performance is not satisfactory. Hence, multiple features are required for effective performance. Second, there is no obvious difference when the radius of LBP descriptor changes or the sampling point changes. Therefore, we

**TABLE IV**  
PERFORMANCE ON BOTH DATABASES WITH VARIOUS TRAIN-TEST SPLITS

Model	Train-Test	TMID [4]		ESPL-LIVE HDR [40]	
		PLCC	SRCC	PLCC	SRCC
Overall	20%–80%	0.6867	0.6071	0.6306	0.6249
Overall	30%–70%	0.7231	0.6515	0.6542	0.6466
Overall	40%–60%	0.7355	0.6617	0.6697	0.6608
Overall	50%–50%	0.7587	0.6825	0.6806	0.6713
Overall	60%–40%	0.7698	0.6925	0.6878	0.6781
Overall	70%–30%	0.8051	0.7230	0.6951	0.6849
Overall	80%–20%	0.8243	0.7321	0.7019	0.6951
Overall	90%–10%	0.8769	0.7619	0.7088	0.6953

reasonably set them as 1 and 8 as the same in other applications. Third, no obvious difference occurs with the  $R_f$  changing, and the performance is slightly superior to others when the  $R_f$  is 11. Hence, we set  $R_f$  as 11 in this paper.

### D. Robustness Analysis

Because the performance of training-based methods is highly determined with respect to the proportion of training images to the whole databases, we need to explore the robustness of the proposed method. To conduct this evaluation, we varied the training portion from 20% to 90%, while that of testing changes from 80% to 10%. The experimental results are given in Table IV. Clearly, we can carefully observe that both criteria (i.e., PLCC and SRCC) gradually increase without drastic changes as the training proportion increases. Moreover, scrupulous readers may find that the performance is still high even though the training set is less than 40%. Specifically, the overall PLCC is 0.7335 and 0.6697 on TMID and ESPL-LIVE HDR databases, respectively. Therefore, we have the confidence to stress that the proposed model is highly robust.

### E. Statistical Performance Evaluation

In order to prove the superiority of the proposed method, we further calculate the statistical significance between it and all competing methods. For this purpose, the two-sample t-test

**TABLE V**  
RESULTS OF TWO-SAMPLE T-TEST PERFORMED BETWEEN PLCC AND SRCC OBTAINED  
BY COMPLETING METHODS ON TWO DATABASES

Database	NIQE	ILNIQE	BIQI	BLIINDS2	GM-LOG	BRISQUE	HOSA
TMID	11	11	11	11	11	11	11
	SISLBM	SSEQ	TCLT	NFERM	NRSL	BSD	FISH
	11	11	11	11	11	11	11
	NIQE	ILNIQE	BIQI	BLIINDS2	GM-LOG	BRISQUE	HOSA
ESPL-LIVE HDR	11	11	11	11	11	11	11
	SISLBM	SSEQ	TCLT	NFERM	NRSL	BSD	FISH
	11	11	11	11	11	11	11

**TABLE VI**

TIME COMPLEXITIES OF IQA METHODS ON TMID DATABASE (IN SECONDS)

Metrics	NIQE	ILNIQE	BIQI	BLIINDS2	GM-LOG
Run time (s)	0.2693	20.2518	0.4549	53.6018	0.0814
Metrics	SISLBM	SSEQ	TCLT	NFERM	NRSL
Run time (s)	2.8734	1.2496	3.2340	51.9645	0.1514
Metrics	BSD	FISH	BRISQUE	HOSA	Proposed
Run time (s)	0.2405	0.7416	0.006	0.4184	5.8917

was employed to measure whether the mean values of two independent samples were equivalent or not. In this paper, the independent sample is the value set of criterion, i.e., PLCC and SRCC, calculated after 1000 train-test splits. The test is conducted at 5% significance level. Table V lists the experimental results on two databases. For simple representation, “1” (“− 1”) indicates that the proposed method is superior (inferior) to the compared method, while “0” means that both methods are statistically equivalent. For each entry, there are two statistical results. For example, the entry “11” (in line two, column two), represents the significance effects on PLCC and SRCC. As expected, the proposed method outperforms all competing methods significantly.

### F. Computational Complexity

In many practical applications, a low-complexity metric is more favored and welcomed. Therefore, we also conduct an experiment to demonstrate the time complexity of the proposed method. For this purpose, we record the run time of the proposed method as well as the completing methods. All algorithms are implemented in MATLAB 2013b and executed on a 2.6 GHz processor with 8 GB RAM, Windows 7 Pro 64-b laptop. For each method, all the images in TMID database are evaluated and total time consumed is recorded by the MATLAB functions. Then, the average processing time per image (in second) is given in Table VI. As Table VI clearly shows, the proposed metric has moderate computational complexity. In addition, we also record the training time consumed during the model learning, and the testing time consumed during tested image quality prediction. Note that both training and testing time do not contain the feature extraction time. As recorded, the training time is 0.5435 s for the whole database, while the testing time is 0.046 ms per image.

### V. CONCLUSION

In this paper, we have presented a biologically inspired blind quality assessment metric of tone-mapped images. As TMOs aim to convert HDR images to LDR images, it is inevitable to lose brightness and chromatic and structural information. With this in mind, we decompose an image into two components by simulating the procedure of color information processing in the brain. Specifically, to obtain textural information, we extract representative features from GLCM computed on the response maps of SO cells; meanwhile, the LBP frequency histograms are extracted from response maps of DO cells to obtain structural information. In addition, the GLCM operator is also conducted on the response maps of DO cells to obtain textural information. At the end, all extracted features and corresponding subjective ratings are utilized to train the module. Extensive experiments have proved that the proposed algorithm outperforms the state-of-the-art NR IQA metrics.

As the multimedia industry begins rapid deployment in both professional and consumer markets, including support for HDR and wider color gamut services is considered essential within the industry. To reduce the data amount of storage on disk and transmission on internet, compression as an effective measurement has been widely used. So far, several compression standards have been proposed for multimedia [47], such as high efficiency video coding, H.264, and moving picture experts group. However, it is inevitable to introduce structure and color distortions during compression, which affects the viewing experience. Therefore, it is of vital importance to develop an objective quality assessment method for providing essential guidance in the generation of compression standards. In the future, we would like to improve the proposed method to account for compressed distortion and try to extend it to solve quality assessment of two-dimensional (2-D) and 3-D video sequences.

### REFERENCES

- [1] E. Reinhard, W. Heidrich, P. Debevec, S. Pattanaik, G. Ward, and K. Myszkowski, *High Dynamic Range Imaging: Acquisition, Display, and Image-Based Lighting*. San Mateo, CA, USA: Morgan Kaufmann, 2010.
- [2] B. Hoefflinger, *High-Dynamic-Range (HDR) Vision*. New York, NY, USA: Springer, 2007.
- [3] F. Drago, W. L. Martens, K. Myszkowski, and H. P. Seidel, “Perceptual evaluation of tone mapping operators,” *Proc. SPIE.*, vol. 5666, pp. 192–203, 2005.
- [4] H. Yeganeh and Z. Wang, “Objective quality assessment of tone-mapped images,” *IEEE Trans. Image Process.*, vol. 22, no. 2, pp. 657–667, Feb. 2013.

- [5] K. Gu *et al.*, "Blind quality assessment of tone-mapped images via analysis of information, naturalness, and structure," *IEEE Trans. Multimedia*, vol. 18, no. 3, pp. 432–443, Mar. 2016.
- [6] W. Lin and C. C. Jay Kuo, "Perceptual visual quality metrics: A survey," *J. Vis. Commun. Image Represent.*, vol. 22, no. 4, pp. 297–312, 2011.
- [7] K. Ma, H. Yeganeh, K. Zeng, and Z. Wang, "High dynamic range image tone mapping by optimizing tone mapped image quality index," *IEEE Trans. Image Process.*, vol. 24, no. 10, pp. 3086–3097, Oct. 2015.
- [8] H. Z. Nafchi, A. Shahkolaei, R. F. Moghaddam, and M. Cheriet, "FSITM: A feature similarity index for tone-mapped images," *IEEE Signal Process. Lett.*, vol. 22, no. 8, pp. 1026–1029, Aug. 2015.
- [9] L. Xie, X. Zhang, S. Wang, X. Zhang, and S. Ma, "Quality assessment of tone-mapped images based on sparse representation," in *Proc. IEEE Int. Symp. Circuits Syst.*, 2016, pp. 2218–2221.
- [10] S. Wang *et al.*, "Subjective and objective quality assessment of compressed screen content images," *IEEE J. Emerg. Sel. Topics Circuits Syst.*, vol. 6, no. 4, pp. 532–543, Dec. 2016.
- [11] R. Soundararajan and A. C. Bovik, "RRED indices: Reduced reference entropic differencing for image quality assessment," *IEEE Trans. Image Process.*, vol. 21, no. 2, pp. 517–526, Feb. 2012.
- [12] A. Mittal, R. Soundararajan, and A. C. Bovik, "Making a "completely blind" image quality analyzer," *IEEE Signal Process. Lett.*, vol. 20, no. 3, pp. 209–212, Mar. 2013.
- [13] L. Zhang, L. Zhang, and A. C. Bovik, "A feature-enriched completely blind image quality evaluator," *IEEE Trans. Image Process.*, vol. 24, no. 8, pp. 2579–2591, Aug. 2015.
- [14] A. K. Moorthy and A. C. Bovik, "A two-step framework for constructing blind image quality indices," *IEEE Signal Process. Lett.*, vol. 17, no. 5, pp. 513–516, May 2010.
- [15] M. A. Saad, A. C. Bovik, and C. Charrier, "Blind image quality assessment: a natural scene statistics approach in the DCT domain," *IEEE Trans. Image Process.*, vol. 21, no. 8, pp. 3339–3352, Aug. 2012.
- [16] W. Xue, X. Mou, L. Zhang, A. C. Bovik, and X. Feng, "Blind image quality assessment using joint statistics of gradient magnitude and Laplacian features," *IEEE Trans. Image Process.*, vol. 23, no. 11, pp. 4850–4862, Nov. 2014.
- [17] Q. Li, W. Lin, and Y. Fang, "BSD: Blind image quality assessment based on structural degradation," *Neurocomputing*, vol. 236, pp. 93–103, 2017.
- [18] K. Gu, G. Zhai, X. Yang, and W. Zhang, "Using free energy principle for blind image quality assessment," *IEEE Trans. Multimedia*, vol. 17, no. 1, pp. 50–63, Jan. 2015.
- [19] Q. Li, W. Lin, J. Xu, and Y. Fang, "Blind image quality assessment using statistical structural and luminance features," *IEEE Trans. Multimedia*, vol. 18, no. 12, pp. 2457–2469, Dec. 2016.
- [20] L. M. Martinez and J. M. Alonso, "Complex receptive fields in primary visual cortex," *Neuroscientist*, vol. 9, no. 5, pp. 317–331, 2003.
- [21] K. R. Gegenfurtner, "Cortical mechanisms of colour vision," *Nature Rev. Neurosci.*, vol. 4, no. 4, pp. 563–572, 2003.
- [22] A. M. Derrington, J. Krauskopf, and P. Lennie, "Chromatic mechanisms in lateral geniculate nucleus of macaque," *J. Physiol.*, vol. 357, no. 12, pp. 241–265, 1984.
- [23] H. J. Dartnall, J. K. Bowmaker, and J. D. Mollon, "Human visual pigments: Microspectrophotometric results from the eyes of seven persons," *Proc. Roy. Soc. London*, vol. 220, no. 1218, pp. 115–130, 1983.
- [24] R. Shapley and M. Hawken, "Color in the cortex single- and double-opponent cells," *Vis. Res.*, vol. 51, no. 7, pp. 701–717, 2011.
- [25] I. E. Abdou and W. Pratt, "Quantitative design and evaluation of enhancement/thresholding edge detectors," *Proc. IEEE*, vol. 67, no. 5, pp. 753–763, May 1979.
- [26] "HDR shop," Inst. Creative Technol., Univ. Southern California, Playea Visra, CA, USA, 2013. [Online]. Available: <http://www.hdrshop.com/>
- [27] J. Zhang, Y. Barhom, and T. Serre, "A new biologically inspired color image descriptor," in *Proc. Eur. Conf. Comput. Vis.*, 2012, pp. 312–324.
- [28] J. P. Jones and L. A. Palmer, "An evaluation of the two-dimensional Gabor filter model of simple receptive fields in cat striate cortex," *J. Neurophysiol.*, vol. 58, no. 58, pp. 1233–1258, 1988.
- [29] R. L. De Valois, E. W. Yund, and N. Hepler, "The orientation and direction selectivity of cells in macaque visual cortex," *Vis. Res.*, vol. 22, no. 5, pp. 531–544, 1982.
- [30] T. Serre, L. Wolf, S. Bileschi, M. Riesenhuber, and T. Poggio, "Robust object recognition with cortex-like mechanisms," *IEEE Trans. Pattern Anal. Mach. Intell.*, vol. 29, no. 3, pp. 411–426, Mar. 2007.
- [31] D. J. Heeger, "Normalization of cell responses in cat striate cortex," *Visual Neurosci.*, vol. 9, no. 2, pp. 181–197, 1992.
- [32] M. Carandini, D. J. Heeger, and J. A. Movshon, "Linearity and normalization in simple cells of the macaque primary visual cortex," *J. Neurosci.*, vol. 17, no. 21, pp. 8621–8644, 1997.
- [33] S. G. Solomon and P. Lennie, "Chromatic gain controls in visual cortical neurons," *J. Neurosci.*, vol. 25, no. 19, pp. 4779–4792, 2005.
- [34] R. M. Haralick, K. Shanmugam, and I. Dinstein, "Textural features for image classification," *IEEE Trans. Syst. Man Cybern.*, vol. SMC-3, no. 6, pp. 610–621, Nov. 1973.
- [35] T. Ojala, M. Pietikainen, and T. Maenpaa, "Multiresolution gray-scale and rotation invariant texture classification with local binary patterns," *IEEE Trans. Pattern Anal. Mach. Intell.*, vol. 24, no. 7, pp. 971–987, Jul. 2002.
- [36] B. Gu, V. S. Sheng, Z. Wang, D. Ho, S. Osman, and S. Li, "Incremental learning for  $\nu$ -support vector regression," *Neural Netw.*, vol. 67, pp. 140–150, 2015.
- [37] A. Mittal, A. K. Moorthy, and A. C. Bovik, "No-reference image quality assessment in the spatial domain," *IEEE Trans. Image Process.*, vol. 21, no. 12, pp. 4695–4708, Dec. 2012.
- [38] L. Liu, B. Liu, H. Huang, and A. C. Bovik, "No-reference image quality assessment based on spatial and spectral entropies," *Signal Process. Image Commun.*, vol. 29, no. 8, pp. 856–863, 2014.
- [39] C. C. Chang and C. J. Lin, "LIBSVM: A library for support vector machines," *ACM Trans. Intell. Syst. Technol.*, vol. 2, no. 3, 2007, Art. no. 27.
- [40] C. A. B. D. Kundu, D. Ghadiyaram, and B. L. Evans, "ESPL-LIVE HDR image quality database," May 2016. [Online]. Available: <http://signal.ece.utexas.edu/debarati/HDRDatabase.zip>
- [41] Z. Wang, A. C. Bovik, H. R. Sheikh, and E. P. Simoncelli, "Image quality assessment: from error visibility to structural similarity," *IEEE Trans. Image Process.*, vol. 13, no. 4, pp. 600–612, Apr. 2004.
- [42] J. Xu, P. Ye, Q. Li, H. Du, Y. Liu, and D. Doermann, "Blind image quality assessment based on high order statistics aggregation," *IEEE Trans. Image Process.*, vol. 25, no. 9, pp. 4444–4457, Sep. 2016.
- [43] P. V. Vu and D. M. Chandler, "A fast wavelet-based algorithm for global and local image sharpness estimation," *IEEE Signal Process. Lett.*, vol. 19, no. 7, pp. 423–426, Jul. 2012.
- [44] K. Gu, G. Zhai, X. Yang, and W. Zhang, "Hybrid no-reference quality metric for singly and multiply distorted images," *IEEE Trans. Broadcast.*, vol. 60, no. 3, pp. 555–567, Sep. 2014.
- [45] Q. Wu, H. Li, F. Meng, and K. N. Ngan, "Blind image quality assessment based on multichannel feature fusion and label transfer," *IEEE Trans. Circuits Syst. Video Technol.*, vol. 26, no. 3, pp. 425–440, Mar. 2016.
- [46] N. Banić and S. Lončarić, "Sensitivity of tone mapped image quality metrics to perceptually hardly noticeable differences," in *Proc. 5th Croatian Comput. Vis. Workshop*, 2016, pp. 15–18.
- [47] E. François, C. Fogg, Y. He, X. Li, A. Luthra, and A. Segall, "High dynamic range and wide color gamut video coding in HEVC: Status and potential future enhancements," *IEEE Trans. Circuits Syst. Video Technol.*, vol. 26, no. 1, pp. 63–75, Jan. 2016.



**Guanghui Yue** received the B.S. degree in communication engineering from Tianjin University, Tianjin, China, in 2014, and he is currently working toward the Ph.D. degree in the School of Electrical and Information Engineering, Tianjin University, China.

His research interests include bioelectrical signal processing, image quality assessment, and three-dimensional image visual discomfort prediction.



**Chunping Hou** received the M.Eng. and Ph.D. degrees in electronic engineering from Tianjin University, Tianjin, China, in 1986 and 1998, respectively.

Since 1986, she has been in the School of Electronic and Information Engineering, Tianjin University, where she is currently a Full Professor and the Director of the Broadband Wireless Communications and 3-D Imaging Institute. Her current research interests include three-dimensional image processing, three-dimensional display, wireless communication, and the design and applications of communication systems.





**Ke Gu** received the B.S. and Ph.D. degrees in electronic engineering from Shanghai Jiao Tong University, Shanghai, China, in 2009 and 2015, respectively.

His research interests include quality assessment and image processing. Dr. Gu is the Associate Editor for the IEEE ACCESS and the Reviewer for 20 SCI Journals. He received the Best Paper Award at the IEEE International Conference on Multimedia and Expo in 2016 and the Excellent Ph.D. thesis Award from the Chinese

Institute of Electronics in 2016.



**Shasha Mao** received the Ph.D. degree in circuit and system from Key Lab of Intelligent Perception and Image Understanding of Ministry of Education, Xidian University, Xi'an, China, in 2014.

Since 2016, she has been a Research Fellow in Nanyang Technological University, Singapore. From 2014 to 2016, she was a Postdoctoral Research Fellow in Singapore University of Technology and Design, Singapore. Her current research interests include deep learning, ensemble learning, low-rank and sparse matrix

factorization, object detection, and face recognition.



**Wenjun Zhang** (F'12) received the B.S., M.S., and Ph.D. degrees in electronic engineering from Shanghai Jiao Tong University, Shanghai, China, in 1984, 1987, and 1989, respectively.

He was one of the main contributors to the Chinese Digital Television Terrestrial Broadcasting Standard issued in 2006 and is leading team in designing the next generation of broadcast television system in China since 2011. He holds more than 40 patents and published more than 90 papers in international journals and

conferences.

Prof. Zhang is a Chief Scientist in the Chinese National Engineering Research Centre of Digital Television, an industry/government consortium in digital television technology research and standardization, and the Chair of Future of Broadcast Television Initiative Technical Committee.